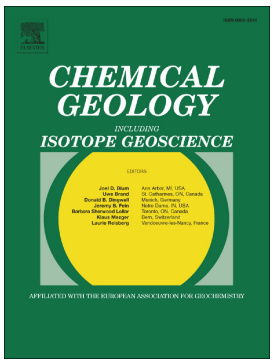

Isobar-free neon isotope measurements of flux-fused potential reference minerals on a Helix-MC-Plus10K mass spectrometer

K.A. Farley, J. Treffkorn, D. Hamilton

PII: S0009-2541(20)30026-7

DOI: https://doi.org/10.1016/j.chemgeo.2020.119487

Reference: CHEMGE 119487

To appear in: *Chemical Geology*

Received date: 4 September 2019

Revised date: 12 January 2020

Accepted date: 31 January 2020

Please cite this article as: K.A. Farley, J. Treffkorn and D. Hamilton, Isobar-free neon isotope measurements of flux-fused potential reference minerals on a Helix-MC-Plus10K mass spectrometer, *Chemical Geology* (2018), https://doi.org/10.1016/j.chemgeo.2020.119487

Isobar-free neon isotope measurements of flux-fused potential reference minerals on a Helix-MC-Plus^{10K} mass spectrometer

K.A. Farley (*Division of Geological and Planetary Sciences, Caltech, Pasadena, CA 91125 USA; farley@caltech.edu*)

J. Treffkorn (*Division of Geological and Planetary Sciences, Caltech, Pasadena, CA 91125 USA*)

D. Hamilton (*Thermo Fisher Scientific, Bremen, Germany*)

Abstract

This work presents new analytical techniques for extraction and analysis of neon from a suite of different mineral phases, including quartz, pyroxene, hematite, apatite, zircon, topaz, and fluorite. Neon was quantitatively extracted at 1100^{o}C from all of these minerals using an in-vacuum lithium borate-flux fusion technique. Evolved neon was purified using a cryogenic method capable of separating Ne from He present in abundances ~8 orders of magnitude higher, typical of samples carrying nucleogenic/radiogenic noble gases. The purified neon was measured on a Helix-MC-*Plus*^{10K} mass spectrometer that permits isobar-free measurement of all three neon isotopes. When operated at its highest mass resolving power (MRP) of ~10,300, the shoulder representing solely ^{22}Ne on the low mass-side of the ^{22}Ne-CO_2^{+2} doublet is wide enough to permit measurement of isobar free ^{22}Ne. Operating in this mode comes with the penalty of a 50% reduction in neon sensitivity. Coupled with a mathematical isobar-

stripping method, this approach excludes 99.5% of the CO_2^{+2} while still collecting >99% of the ^{22}Ne beam. Routine edge-centering on the dynamic CO_2^{+2} peak prior to introduction of a sample permits rapid and robust relocation of the desired measure point in the mass spectrum.

Cosmogenic ^{21}Ne and ^{22}Ne concentrations obtained using these methods on the Cronus-A quartz and Cronus-P pyroxene international reference materials are in excellent agreement with previous work or expectations. Similarly, the concentration of nucleogenic ^{21}Ne and ^{22}Ne in Durango apatite and the CIT hematite standard agree well with previous work. Durango apatite has notable heterogeneity in neon concentrations, consistent with previous observations of heterogeneous He, U and Th concentrations in this apatite. Nucleogenic neon concentrations are also presented for previously unstudied minerals including a Sri Lanka zircon (SLC), a topaz from the Imperial Topaz mine in Brazil (ITP1), and a fluorite (W-90) from New Hampshire. Taken together this set of potential reference minerals and the associated dataset provide a starting point for intercalibration among multiple mineral phases carrying ^{21}Ne and ^{22}Ne of cosmogenic or nucleogenic origin.

1. Introduction

Neon in minerals is derived from multiple sources of interest in geochemistry and geochronology. For example, both ^{21}Ne and ^{22}Ne are produced by cosmic-ray-induced nuclear spallation of common target elements such as Mg, Al, and Si, permitting surface

exposure dating of quartz, olivine, and pyroxene (Niedermann, 2002). Alpha-particle capture reactions on ^{18}O and ^{19}F produce measurable quantities of ^{21}Ne and ^{22}Ne, respectively, allowing radiometric dating of many phases (Cox et al., 2015; Gautheron et al., 2006) including some that are not typically datable, such as hematite and fluorite (Farley and Flowers, 2012; Sole and Pi, 2006). Finally, many minerals carry trapped neon components. While trapped modern atmosphere is considered a nuisance for most neon isotope applications, neon trapped in fluid inclusions in mantle-derived minerals and in basaltic glass provides unique insights to mantle evolution (Honda et al., 1991; Peron et al., 2019; Sarda et al., 1988).

This paper addresses several challenges associated with accurate and routine measurement of neon isotopes in minerals. First, during mass spectrometric measurement of neon, common instrumental background species create isobaric interferences. For example, $^{40}Ar^{+2}$, HF, and $H_2{}^{18}O$ are isobaric with ^{20}Ne, ^{20}NeH is isobaric with ^{21}Ne, and $CO_2{}^{+2}$ is isobaric with ^{22}Ne (Niedermann et al., 1993; Wielandt and Storey, 2019). Recent advances in mass spectrometer design have improved mass resolution enough to eliminate all but the $CO_2{}^{+2}$ isobar (e.g., Wielandt and Storey, 2019; Zhang et al., 2016), which has the same mass as ^{22}Ne to closer than 1 part in 6,000. Here we describe a new version of the ThermoFisher Helix-MC, called the *Plus*^{10k}, that has sufficient mass resolving power to almost completely eliminate even the $CO_2{}^{+2}$ isobar.

A second challenge in neon measurement of geologic samples is a lack of analytical methods capable of quantitatively extracting neon from multi-mg to gram samples of

minerals. While laser methods achieve extremely high temperatures that likely can extract neon from any mineral, they are not readily scaled to large sample mass. Especially for cosmogenic dating in which neon concentrations are typically low, analysis of large samples is essential. While resistance furnace methods are better-suited to large mass samples, at the high temperatures necessary to quantitatively extract neon, furnaces often have high analytical blanks and may not survive long. This paper describes a generally applicable flux-fusion technique that quantitatively extracted neon from every mineral we analyzed, at 1100^{o}C.

A final challenge, unique to the analysis of nucleogenic neon, is isolation of small quantities of neon from overwhelmingly more abundant helium. Instrument sensitivity and mass bias for neon are affected by the presence of helium (Hiyagon, 1989), so accurate measurements require purified neon. Here we describe a cryogenic technique that adequately isolates neon even in samples with a $^{21}Ne/^{4}He$ ratio of ~$5x10^{-8}$.

2. Helix MC *Plus*^{10K} Instrument Description

The HELIX MC *Plus*^{10K} static vacuum mass spectrometer is a magnetic sector instrument designed principally for the isotopic analysis of small samples of the noble gases. It comprises a magnetic sector analyzer with 35cm, 120-degree extended geometry ion optics. The analyzer includes two ion optical elements for peak optimization. The first element is a "multipole" lens, located immediately after the ion source, which permits tuning of the ion beam for sensitivity and peak shape. The second element is a "flatapole"

lens located before the ion beam enters the main magnet. This lens is used to optimize resolution and resolving power over the focal plane.

The ion source optics incorporates an assembly that enables selection among defining slits with widths of 0.25, 0.05 or 0.025 mm. Narrower defining slits give higher mass resolving power at the expense of sensitivity. Here mass resolving power refers to the steepness of the edge of an ion peak, defined as m/Δm where m is the m/e ratio of the peak and Δm is the difference in mass between the 5% and 95% peak heights of one side of the peak. The mass resolving power of the smallest slit, up to 10,000, was designed to enable the partial separation of ^{22}Ne from its $^{12}C^{16}O_2^{+2}$ interference. All work described here was done with the smallest (0.025mm, HR mode) defining slit.

Five detectors are aligned in the focal plane of the HELIX MC *Plus*^{10K} , and from low mass to high mass are referred to as L2, L1, AX, H1, and H2. Each of these detectors contains both a voltage suppressed Faraday bucket and an ion-counting compact discrete dynode (CDD) multiplier. The axial detector (AX) is fixed, while the positions of the two detectors to each side are adjustable. The ion entry slits for all detectors except L1 have a width of 0.6 mm giving a mass resolution of ~750 (10% peak height definition). L1 has an entry slit width of 0.3 mm giving a mass resolution of ~1500. The resolution of the L1 detector is adequate to resolve not only the low mass $^{40}Ar^{+2}$ interference but also the high mass HF and $H_2{}^{18}O$ interferences from ^{20}Ne (e.g., see Niedermann et al., 1993). It should be noted that in this particular case, with isobars bracketing both sides of the peak of interest, high mass resolving power is not sufficient to allow isolation of the single

desired peak. This is because at 750 resolution there is no magnetic field setting where only ^{20}Ne enters the detector; in sweeping the magnetic field to higher mass starting on the low mass edge of ^{20}Ne, first both ^{20}Ne and $^{40}Ar^{+2}$ would pass through the slit, and before $^{40}Ar^{+2}$ completely exits the slit, the HF-$H_2{}^{18}O$ peak enters. This problem can only be solved by a narrower slit just in front of the detector that permits admission of only the desired ^{20}Ne beam (yielding 1500 mass resolution). The narrow entry slit on L1 provides a narrower peak-flat, but does not affect sensitivity because the entire beam passes through it.

3. Methods

3.1 Standard gas

For neon, we use a calibration gas consisting of a tank and pipette system that delivers ~$6x10^{-6}$ cm^3 STP of untreated air to the extraction line. The volume of the tank (~4000 cm^3) and pipette (~1 cm^3) were calibrated using a capacitance manometer and a glass bulb whose volume was determined with high accuracy by weight after filling with mercury. These data were used to determine the volume of the air aliquot delivered and also to estimate the tank depletion rate. This tank currently delivers $90x10^{-12}$ cm^3 STP of ^{20}Ne (4.1 fmol). There are two recent determinations of the neon isotopic composition of air (Honda et al., 2015; Wielandt and Storey, 2019). These determinations are in agreement with each other and with previous work (Eberhardt et al., 1965) with respect to the $^{22}Ne/^{20}Ne$ ratio (0.102), but they differ significantly in $^{21}Ne/^{22}Ne$ ratio. We adopt the more thoroughly established ratio reported by Wielandt and Storey (2019): 0.029577. If

we were to adopt the $^{21}Ne/^{22}Ne$ ratio of Honda et al. (2015), our reported ^{21}Ne excesses would be about 1.8% lower. The He content of this tank was augmented by the introduction of both ^{3}He and ^{4}He, yielding a $^{3}He/^{4}He$ ratio of 2.03 R_A and a per-shot delivery of ~$70x10^{-9}$ ccSTP.

For some aspects of instrument tuning we used a ^{22}Ne isotope spike that delivers $450x10^{-12}$ cm^3 STP (Cox et al., 2015). This gas was used because of its high neon abundance compared to the air standard, rather than because of its isotopic purity. It has no ^{4}He.

Helium is known to influence neon isotopic measurements in Nier-type ion sources, presumably arising from space-charge effects (Hiyagon, 1989). The simplest solution to this problem is to separate Ne from He prior to Ne inlet to the mass spectrometer. Because our samples often have vastly lower $^{21}Ne/^{4}He$ ratios than our standard ($^{21}Ne/^{4}He$~$4x10^{-5}$), we found it useful to create a tank of working gas containing nucleogenic He and Ne with a $^{21}Ne/^{4}He$ ratio of ~$5x10^{-8}$. We created this gas by loading approximately 1 gram of a Sri Lanka zircon, age ~ 540 Ma (e.g., Nasdala et al. (2018)) into a double-walled vacuum resistance furnace along with 10 grams of lithium borate flux (see details on furnace extractions, below). The gas bottle, with manual pipette system, was attached directly to the furnace. After pumpdown, the zircon-flux mixture was fused and the evolved gas expanded into the tank. Quantitative extraction was not demonstrated, but for our purposes it was not required. This same zircon-sourced gas was recently used to demonstrate detection of fission Kr and Xe on a custom-built ion trap

mass spectrometer (Avice et al., 2019). We here refer to this working gas as "zircon-in-a-bottle", ZIB.

3.2 Instrument operation for isobar-free measurement of Ne isotopes

The general procedure for setup and analysis of neon isotopes on the Caltech Helix MC *Plus*^{10K} is shown in Figure 1. Because the somewhat unusual setup for separation of ^{22}Ne from CO_2^{+2} has not previously been reported, each step is described in detail below.

3.2.1 Ion Source Tuning

The Helix MC *Plus*^{10K} has 11 adjustable ion source controls (Table 1). Seven of these controls require tuning when operating in low resolution mode and are typically optimized for peak intensity. The remaining four are adjusted to maximize mass resolving power in HR mode.

We developed an automated procedure to facilitate tuning for peak intensity and, with a small modification, for mass resolving power. Rather than iteratively maximizing the signal for each lens setting individually and manually, we used an automated gradient maximization approach. We used the Nelder-Mead algorithm (Nelder and Mead, 1965), which is designed to find the maximum of a function of many variables. For our application the variables are the source controls, and the function being optimized is either the peak height or mass resolving power response of the instrument. We started

with a publicly available Labview implementation of the Nelder-Mead algorithm available on Github, and we replaced the subroutine that evaluates the value of the mathematical function being maximized with routines to set lenses, read the mass spectrometer detectors, and return the peak height. For the low resolution lens tuning, we simply maximized the ^{20}Ne peak height of an air standard on L1. This approach typically located the sensitivity maximum in about 20 minutes without user intervention. Rerunning the algorithm from a different starting tune set always yielded the same final optimized set, suggesting that the global maximum was located.

For optimization of mass resolving power (MRP), we introduced 4 shots of the ^{22}Ne spike into the instrument. We used this large amount of ^{22}Ne to ensure that any isobaric CO_2^{+2} did not corrupt the MRP determination. This optimization could also have been made using the air standard, though many more aliquots would be required to get sufficient ^{22}Ne (i.e., signal intensity is important but isotopic purity is not). To measure MRP, we magnetically scanned the leading edge of the ^{22}Ne peak, typically in 50 steps of about 1 mAMU each. We then computed MRP (5%-95% definition) and let the algorithm iteratively maximize this quantity by adjusting the high resolution lenses followed by a peak scan. We typically achieved a mass resolving power of slightly over 10,000 (Table 1). This procedure takes several hours because the magnetic field scan is time consuming. Perturbing the initial condition always yielded the same final tune set or one with identical MRP; we found a strong correlation between optimal rotation quad – flatapole lens settings. Optimization of the high resolution lenses made no discernable difference to sensitivity.

Typical lens settings used in the course of this work are included in Table 1.

3.2.2 Determination of ^{22}Ne Measure Point

A typical isotope ratio measurement on a multi-collector mass spectrometer involves positioning of the detectors close to the center of each peak. In contrast, the goal of the HR neon measurement described here is to largely eliminate the CO_2^{+2} isobar on ^{22}Ne, i.e., to make the measurement on the narrow low-mass-side "bench" on the ^{22}Ne-CO_2 doublet that is purely ^{22}Ne (Figure 2). Here we describe how we set up the instrument, identified the magnetic field measure point, maintained high stability in the location of this point throughout an analytical session, and corrected for the small amount of CO_2^{+2} remaining at the measure point.

If very large amounts of neon are analyzed, it may be possible to determine by inspection of the Faraday peak shape the location of the isobar-free portion of the doublet. However, typical ^{22}Ne levels in many samples we wish to analyze (and in our air standard) are so small that we must use a CDD. At beam intensities of <100 kcps, the bench is not obvious (Figures 2, 3); for comparison our air standard delivers only ~2.2 kcps of ^{22}Ne.

We used simultaneous detection of ^{20}Ne, ^{21}Ne, ^{22}Ne, and the $^{45}CO_2^{+2}$ isobar on the CDDs referred to as L1, AX, H1, and H2, respectively. The first step in the setup process (Figure 1) is to use an air standard to get these detectors in their approximate position.

On the Caltech Helix MC *Plus*^{10K}, the dynamic mode CO_2^{+2} is typically 150 cps (on H1) which corresponds to 1-2 cps of $^{45}CO_2^{+2}$ on H2. This is adequate to place the H2 detector in its appropriate position.

To identify the magnetic field setting of the optimal ^{22}Ne measure point, we started with the following arbitrary but reasonable objectives to be fulfilled simultaneously. 1) The ^{22}Ne beam height should be within 1% of its maximum. This requirement sets the lower bound on the magnetic field setting of the measure point (any lower and one is falling off the low mass side of the peak). The 99% point was established by scanning the leading edge of a gas standard (the ^{22}Ne spike) with abundant ^{22}Ne, to minimize any impact of isobaric CO_2 (Figure 3a). 2) At the measure point, at least 90% of the CO_2 beam should be rejected. This sets the high mass limit of the measure point because going to higher mass admits more of the isobar. We established the location where the CO_2^{+2} peak reaches 10% of its maximum value by scanning the leading edge of the CO_2^{+2} peak in dynamic mode (i.e., vacuum pump open, Figure 3a). Combining these two limits we found a target zone for the measure point that is ~1 mAMU wide (Figure 3b). Near the center of this target region ~95% of CO_2^{+2} is rejected, we call this magnetic field point M_R.

One mAMU is a narrow magnetic field range, and to prove that it is feasible to locate and maintain such a narrow target, we measured the instrument's peak-side stability. We found that over a 1 hour period, the peak drift is <0.2 mAMU, or about 5 times better than we require to complete a 1 hour measurement without drifting out of the target zone.

Interestingly, this corresponds to a peak side stability of ~ ±5 ppm, substantially better than the Helix MC *Plus*^{10K} specification (±25 ppm for ^{40}Ar). We noticed that laboratory temperature fluctuations can substantially degrade peak-side stability.

At this point we have all the information required to precisely position the detectors. With the magnetic field set at M_R, H1 will be positioned correctly to measure nearly isobar-free ^{22}Ne (Figure 2). The AX and L1 detector positions now need to be touched-up such that ^{20}Ne and ^{21}Ne are centered and free of isobars (e.g., of $H_2{}^{18}O$, HF, and ^{20}NeH (Wielandt and Storey, 2019; Zhang et al., 2016). Note that since the AX detector is not movable, it may be necessary to move H1 and relocate M_R such that ^{21}Ne is appropriately centered. It is also possible to adjust the effective position of the detectors using the CDD deflection controls, though we did not use this approach. For reasons discussed below, we also position H2 such that $^{45}CO_2{}^{+2}$ is centered at M_R.

Over timescales longer than a few hours, it is clear that magnetic field instability will cause the target region in the mass spectrum to drift away from the specified measure point M_R. Therefore we require a method to relocate the measure point at a regular cadence during an analytical session. Fortunately, all of the necessary information to relocate the measure point is contained within a dynamic mode $CO_2{}^{+2}$ peak scan on H1.

To use this scan it is first necessary to establish the magnetic field offset (ΔM) between a readily located part of the dynamic $CO_2{}^{+2}$ peak, and the measure point (M_R, Figure 3a). The steepest portion of the $CO_2{}^{+2}$ peak is most diagnostic of a specific location in the

mass spectrum, and the steepest part roughly corresponds to the 50% intensity point. On the Caltech Helix MC the dynamic CO_2^{+2} beam is remarkably stable in intensity over many week periods, at about 180 cps. Thus by simply scanning up the low mass side until a peak height of 90 cps is obtained, it is possible to quickly and precisely relocate the mass spectrum. We refer to this magnetic field position as M_C. Then, because the measure point is defined by the fraction of the CO_2^{+2} peak that is rejected (i.e., 95% at M_R), we can use a single long-integration-period dynamic scan to determine the magnetic field offset ΔM between the 50% point and the 5% point, $\Delta M = M_C - M_R$.

With this information we can now transition from setup mode to analysis mode for a given analytical session. To prevent magnetic field drift out of the ^{22}Ne target zone, between each analysis we scan the dynamic mass spectrum to relocate the 50% point of the low mass side of the CO_2^{+2} peak on H1 (i.e., we relocate M_C). We then set the magnetic field to $M_C - \Delta M$, which places the magnetic field at the relocated measure point M_R. (To be clear, we could also simply have relocated to the 5% point on the dynamic CO_2^{+2} peak, but it is challenging to accurately locate such a low intensity part of the CO_2^{+2} edge).

There is one final step that allows mathematical rejection of the ~5% of the CO_2^{+2} isobar remaining at M_R. By measuring the $^{45}CO_2^{+2}$ isobar on H2, we have a tracer of how much CO_2 is in the instrument during an analysis (Wielandt and Storey, 2019). The amount of CO_2 in the instrument can vary through time during an analysis; for example, we often see a transient rise and decay of this isobar associated with closure of the inlet valve at

the start of an analysis. We can use the signal on H2 to correct for even the small amount of CO_2^{+2} that remains at M_R if we know the relative intensities of the CO_2 isotopologues on H1 and H2. Because we are measuring off to the side of the CO_2^{+2} peak on H1 (Figure 3a), we cannot assume the canonical isotopic ratios to establish the relative intensities on H1 and H2. Instead, after relocating M_R as described above, we briefly close the mass spectrometer and measure the ratio R_{CO2}=H1/H2. By tagging R_{CO2} in to the data file associated with the analyses that follow, we can make an after-the-fact correction to the ^{22}Ne isotopic evolution in the mass spectrometer during those analyses, i.e., ^{22}Ne=H1-R_{CO2}*H2. This final step ensures that even the 5% of CO_2^{+2} that was not rejected is removed computationally. Furthermore, because the measurement is made every cycle of an analysis, any time-variation in the amount of CO_2 in the instrument during an analysis can be accurately tracked and removed. Based on H2 observations in dynamic and static modes, we found that the mass spectrometer typically has about 3 times higher CO_2 pressure with the pump closed, i.e., about 450 cps of CO_2^{+2} . This provides further impetus to make the correction based on the measured H1/H2 ratio rather than simply subtracting the dynamic blank level on H1 at M_R.

We verified that this edge-scanning method reliably relocates the measure point M_R by running the relocation program continuously for 6 hours. For this experiment we assumed that the mass spectrum is not drifting over the duration of the experiment. We found that the edge scanning routine indicates peak drift of about 0.2 mAMU, comparable to the peak-side stability figure and confirming that relocation is as accurate as reasonably expected.

4. Gas Handling

The procedure described below was designed to purify and cryo-concentrate neon prior to inlet into the mass spectrometer. Special attention was paid to the need to separate a very small amount of neon from very much larger amounts of He as is required for studies of nucleogenic neon ($^{21}Ne/^{4}He$ production ratio ~$5x10^{-8}$ e.g., Cox et al. (2015); Gautheron et al. (2006); Yatsevich and Honda (1997)).

At the beginning of each analysis (standard introduced from standard bottle or sample introduced from furnace), a cryogenic cold head custom built by Janis Research was heated to 200 K for 20 minutes and pumped to the ion pump to clean the charcoal. This step was found to be very important in getting repeatable efficiency of transfer of neon into the mass spectrometer. After this bakeout, the cryogenic trap was set to 26 K and isolated from the vacuum line. Neon gas to be analyzed was then introduced into the vacuum system and sequentially exposed to hot and cold SAES getters to remove active species and a liquid nitrogen trap with charcoal to eliminate argon. The latter was implemented to reduce competition for sorption on the cryogenic system charcoal and to minimize the amount of Ar inadvertently introduced into the mass spectrometer during the neon analysis.

The next step in the process was optimized and verified using the ZIB gas (section 3.1). The goal was to quantitatively transfer neon to the cryogenic system and to leave all or at

least most of the He in the gas phase so it can be pumped away. If the temperature of the charcoal in the cryogenic system is too low in this step, the enormous abundance of He may outcompete neon for sorption on the charcoal, and some of the neon may fail to be transferred. At too high a charcoal temperature some of the neon may not sorb at all, or may be only weakly sorbed, such that that it may be pumped away with the He. Thus this temperature is critical. We exposed separate aliquots of the ZIB gas (purified as described above) to the cryogenic system for 10 minutes at temperatures ranging from 22 to 30 K. At the end of this period we pumped on the charcoal with a turbomolecular pump for 5 minutes to remove the He. We found that at 26 K very little He or Ne remained in the gas phase at the end of this process, and upon heating of the charcoal to the neon release temperature of 78 K, no additional He was released. This suggested that 26 K was an appropriate temperature to separate helium from neon. As an additional test, we analyzed the ^{22}Ne spike gas either by itself (no He present) or with an aliquot of ZIB mixed with it (abundant He present). ZIB has no excess ^{22}Ne, so this mixture provides an excellent test for quantitative transfer of ^{22}Ne. At 26 K, we saw no difference in the excess ^{22}Ne abundance with and without the ZIB gas and its associated ^{4}He. Further experiments confirmed this behavior for variations of ±1 K in the charcoal temperature and for doubling the duration of the He pump-off step. Thus these conditions appear to be robust against small procedural variations.

Based on these results, we exposed the analyte gas to the cryogenic system at 26 K for 10 minutes, then pumped He away to the turbomolecular pump for 5 minutes. We then

raised the temperature of the charcoal to 68 K, at which point the neon was admitted into the mass spectrometer for analysis.

5. Sensitivity, Reproducibility, Linearity

We measured sensitivity using single shots of the air standard. The sensitivity we report is for ^{21}Ne, but in practice we compute sensitivity for all three isotopes separately given the likelihood of instrumental mass bias and varying CDD response.

Neon sensitivity was typically 2.7×10^{14} cps/cc STP (~2.1×10^{-4} A/Torr), equivalent to ~75 cps of ^{21}Ne on a single shot of the air standard. This is about 45% of the sensitivity we obtained with the largest (0.25 mm) defining slit (LR mode). Reproducibility of Ne peak heights over several-day periods was typically between ~0.7 and 1% (1 standard deviation) for all three isotopes. The fact that all three isotopes yield about the same precision despite orders of magnitude variation in beam intensity indicates that factors other than counting statistics control reproducibility. For reference, with our 40 minute integration time, counting statistics limit precision to 1% at a count rate of just 3 cps, compared to the 75 cps of ^{21}Ne in our air standard. It is unclear whether the observed variability arises from mass spectrometer instability or from variations in neon transfer efficiency during purification. We found that it was beneficial to retune the instrument approximately weekly.

Figure 4 shows the linearity of the peak height response in HR mode. This figure indicates no detectable variation in sensitivity across 1.7 to 76 kcps of ^{20}Ne, equivalent to $7x10^{-12}$ to $3x10^{-10}$ cc STP of neon. All results described below are within this abundance range. Zhang et al. (2016) noted nonlinear peak height response of neon in the ANU HELIX MC; we do not observe similar behavior on the Caltech HELIX MC-*Plus*^{10K}.

6. Solid Sample Analysis

6.1 Samples

We selected a variety of different minerals to assess the capabilities of a flux-based neon extraction method coupled with HELIX MC *Plus*^{10K} mass spectrometry. The samples were also selected to provide a useful intercomparison of nucleogenic or cosmogenic neon concentrations among existing or potential reference materials. The mass of material and grain size analyzed for each mineral is listed in Table 2.

Samples we analyzed include:

1) Durango Apatite "C". This megacrystic apatite yields a (U-Th)/He age of 31.6 Ma and is a widely used reference material for geochronology (McDowell et al., 2005). We used the "Durango C" material prepared by Cox et al. (2015).

2) Cronus-A Quartz. This internationally distributed Antarctic quartz sample has a very high cosmogenic neon concentration and was included in a recent study of inter-laboratory variability in cosmogenic neon measurements (Vermeesch et al., 2015).

3) Cronus-P Pyroxene. This internationally distributed Antarctic pyroxene was the focus of a recent inter-laboratory comparison of cosmogenic helium concentration measurements (Blard et al., 2015). To our knowledge the cosmogenic neon concentration of this material has not previously been reported.

4) CIT Hematite. This reference material was prepared from a large specimen of "pencil ore" hematite from Gogebic, Michigan. It was previously analyzed for Ne and reported as sample MI-43 by Farley and McKeon (2015). We now use this material routinely to monitor performance when analyzing nucleogenic neon.

5) SL1 Zircon. This material was prepared from a commercially acquired zircon megacryst from Sri Lanka. Although previous geochronology has been undertaken on samples from this well-known locality (Nasdala et al., 2018), this particular megacryst has not previously been analyzed.

6) ITP Topaz "A". This cm-size topaz specimen, obtained from the Caltech mineral collection, originates from the Imperial Topaz Mine, Ouro Prieto, Minas Gerais, Brazil (Olsen, 1971). No previous work has been done on this specimen, nor to our knowledge on neon in topaz from this or other localities.

7) W-90 Fluorite. This light green fluorite specimen, obtained from the Caltech mineral collection, originates from fluorite deposits in Westmoreland, New Hampshire, USA (Young, 1990). No previous work has been undertaken on this specimen nor to our knowledge on other fluorites from this locality.

6.2 Noble Gas Extraction Method

Here we thoroughly describe a flux-melting-based extraction technique that we first introduced for hematite geochronology (Farley and McKeon, 2015). While laser heating is usually the method of choice for noble gas extraction from small samples (typically <few mgs), laser heating of larger samples is challenging. For example, we have observed inhomogeneous heating, self-shielding, and grain hopping when trying to laser-heat large samples. The laser-heated microfurnace technique (House et al., 2000) eliminates some of these problems for samples up to a few mg, but at the high temperatures likely necessary for neon extraction from minerals like zircon, the encapsulating metal tube (Pt, Nb) frequently fails. For this reason we rely on a double-walled resistance furnace for extraction from large masses of material (5 mg to few grams).

It is generally known that noble gas extraction blanks increase with temperature in a resistance furnace. In addition, while our Heine-type resistance furnace can achieve a maximum temperature of ~1800^{o}C, neither the heater element nor the crucible and liner

survive long under these intense conditions. As an alternative, we use lithium borate flux to lower the melting point of the minerals being extracted.

Approximately 3 grams of 70-30 lithium metaborate-lithium tetraborate is loaded into a molybdenum liner seated in a niobium crucible in the resistance furnace. Multiple samples, each wrapped in tin foil, are loaded in a holder attached to a magnetically coupled linear drive mechanism above the furnace, from which the samples can be sequentially dropped into the furnace. The assembly is pumped to UHV with a turbomolecular pump, and the furnace is heated to ~1200^{o}C for about 1 hour to degas the flux. This initial heating step must be done slowly to prevent violent bubbling upon first melting of the flux. Prior to analysis samples are heated in the vacuum line to 75^{o}C for at least 12 hours to drive off loosely bound noble gases.

To extract gas from a sample, the sample ball is pushed out over the opening to the furnace, and falls into the (cold) liner filled with now-frozen flux. The furnace is heated over a period of 5 minutes to a set point of 1100^{o}C, and is held for 30 minutes to fuse the flux and sample, releasing noble gases. The furnace is then allowed to cool for 5 minutes prior to inlet into the vacuum line. These temperatures and times were developed empirically by repeated extractions that demonstrate complete release of sample neon (and helium). Up to a dozen samples can be dropped into the flux for extraction and analysis, one after the other. Sometimes the flux climbed a short distance up the sides of the Mo liner and formed a partial or total plug. We found that this plug can usually be

melted away by brief heating of the furnace to higher temperatures. Molybdenum liners can be bored out with a drill to resuse them once they become full of flux and sample.

A second extraction of every sample was performed at the same furnace temperature. In every case no neon above the hot blank (and no excess ^{21}Ne or ^{22}Ne) were detected. This demonstrates the efficacy of the flux in liberating neon from a wide range of minerals.

7. Results

7.1 Blanks and elimination of CO_2 isobar

In this section we demonstrate the efficiency with which the CO_2^{+2} isobar is removed using a batch of 36 furnace hot blanks run over a several week period. These blanks were analyzed as described in the previous sections. The yield of ^{20}Ne ranged from undetectable above the line blank, to about $3x10^{-12}$ cm^3 STP. Higher blanks were usually associated with an inadequately pumped furnace/sample chamber. By assuming that all blank neon is isotopically air-like, we can use the measured ^{20}Ne to compute the associated ^{22}Ne blank, and then subtract it from the measured mass 22 (^{22}Ne + residual CO_2^{+2}). While this assumption may not be completely correct (e.g., because the blank may be isotopically fractionated), it provides a simple estimate of the remaining CO_2^{+2} isobar being measured.

As shown in Figure 5, across a broad range of ^{20}Ne blank, the amount of mass 22 that is not accounted for by ^{22}Ne ranges from +0.025 to -0.025x10^{-12} cc STP of neon equivalent. The mean and standard deviation are 0.006 ± 0.011 x10^{-12} cc STP. Stated differently, of the ~450 cps of CO_2^{+2} that are present in the middle of the ^{22}Ne-CO_2^{+2} doublet, the technique described here removes all but 1.2 ± 2.3 cps (or 99.7%). Of this, 95% is removed by the high mass resolving power of the instrument, and the rest by mathematical isobar stripping.

For the samples described below we did not make furnace hot blank corrections. Instead, we subtracted a line blank (usually ~0.3x10^{-12} cc STP ^{20}Ne), and then computed the amount of ^{21}Ne and ^{22}Ne in excess of atmospheric neon. This lumps together atmospheric neon in the furnace blank with any trapped atmospheric neon in the samples.

7.2 Analytical results on potential reference materials

Results of the sample analyses are listed in Table 2 and compared with previous work on the same material (if any) below. Table 2 includes measured neon amounts and isotope ratios, as well as the excess components of ^{21}Ne and ^{22}Ne, i.e., the amount of these isotopes present after correction for air addition assuming that all ^{20}Ne is air-derived (e.g., Niedermann (2002)). Excess concentrations, rather than absolute concentrations, are most relevant for intercomparison of reference materials because the amount of atmospheric neon can vary from aliquot to aliquot of the same sample. It should be explicitly noted that the assumption that all ^{20}Ne is air derived is not fully correct, as both cosmic ray

spallation and neutron capture on oxygen can produce this isotope. Nevertheless, for intercomparison of neon concentrations among different minerals, air excesses are sufficient to characterize a given specimen.

CRONUS-A Quartz

We obtained highly reproducible ^{21}Ne excesses on three aliquots of CRONUS-A quartz, with a mean and standard deviation of 0.551±0.001 fmol/g. This precision exceeds our estimated accuracy on the neon standard calibration, which is uncertain at about the 1% level. Thus our best estimate of the ^{21}Ne excess in CRONUS-A is 0.551±0.006 fmol/g, equivalent to 332 ± 4 million atoms per gram (Mat/g). Previous workers reported values in the range 330-338 Mat/g for CRONUS-A (Vermeesch et al., 2015), in excellent agreement with our result. We obtained an excess ^{22}Ne/^{21}Ne ratio of 1.22 ± 0.13. Because some ^{20}Ne is cosmogenic, the excess ratio is not identical to the cosmogenic ^{22}Ne/^{21}Ne production ratio. Instead, it is the slope of the cosmogenic addition line in neon 3-isotope space (Niedermann, 2002). Previous workers have suggested a statistically identical but slightly shallower slope for cosmogenic neon in quartz, e.g., 1.108 ± 0.007 (Vermeesch et al., 2015).

CRONUS-P Pyroxene

This Antarctic pyroxene yielded reproducible ^{21}Ne and ^{22}Ne excesses of 2.41±0.02 and 2.70±0.07 fmol/g, respectively, corresponding to 1448±14 and 1625±39 Mat/g of cosmogenic neon. Previous work on this material indicates a mean cosmogenic ^{3}He concentration of 5020 Mat/g (Blard et al., 2015), but did not report neon concentrations.

Combining this ^{3}He value with our ^{21}Ne result indicates a ^{21}Ne/^{3}He production ratio of 0.29. This ratio is sensitive to the composition of the target mineral, and the result presented here is in the range of those previously reported for pyroxene (Fenton et al., 2009; Schafer et al., 1999). Our measured excess ^{22}Ne/^{21}Ne ratio of 1.12 ± 0.03 is again in statistical agreement with, but slightly higher than, previous work on this mineral (e.g., 1.069±0.035, (Schafer et al., 1999)).

CIT-10443 Hematite

Eight aliquots of this hematite yielded a mean excess ^{21}Ne concentration of 0.905 fmol/g with a standard deviation of 0.033 fmol/g (3.7%). These results are overdispersed relative to the analytical error, with an MSWD value of 8.4. It is unknown whether this represents true variability within the ~20 mg aliquots analyzed, or unknown additional sources of analytical error. Farley and McKeon (2015) reported an excess ^{21}Ne concentration on a different split of the same hand sample of 0.904 ± 0.017 fmol/g, indistinguishable from the new result.

Our data suggest a small excess of ^{22}Ne in this sample (average 0.081 ±0.026 fmol/g). Capture of α particles by oxygen does not produce ^{22}Ne, but capture on ^{19}F does. Using the nucleogenic production rates from Cox et al. (2015), this amount of ^{22}Ne could be produced from about 2 ppm of F in the hematite. Although this much F in hematite seems unlikely, it could also be present in trace mineral inclusions.

Durango Apatite C

Four aliquots of Durango apatite yielded excess neon concentrations of 0.384 ± 0.017 (4.4%) and 9.13 ± 0.38 (4.1%) fmol/g for ^{21}Ne and ^{22}Ne respectively. The only previous measurement of Durango apatite of which we are aware is from Cox et al. (2015): 0.406 ± 0.004 and 8.74 ± .09 fmol/g. Our new neon results scatter more than expected from known analytical uncertainties, with MSWD values of 7 and 4 for ^{21}Ne and ^{22}Ne. Cox et al. (2015) also found greater than expected variability in the excess Ne concentrations of Durango apatite. These observations suggest that the heterogeneity observed by Boyce and Hodges (2005) in U (10-15 ppm) and Th (203-329 ppm) in Durango apatite is not averaged out in aliquots of even 10's of mg of ~150μm diameter grains.

SL1 Zircon

Two aliquots of this zircon sample yielded 70.0 ± 0.7 fmol/g of ^{21}Ne, by far the highest excess neon concentration in the dataset. As with the CIT hematite, there is detectable excess ^{22}Ne, ~ 1.0±0.3 fmol/g. This much ^{22}Ne could arise from ~300 ppb of F in the zircon or in mineral inclusions.

W-90 Fluorite and ITP-A Topaz

Two aliquots of New Hampshire fluorite W90 yielded no detectable ^{21}Ne (<0.0002 fmol/g), as expected for this oxygen-free (CaF_2) phase. The ^{22}Ne concentration of 0.34 ± 0.02 fmol/g was also surprisingly low, suggesting a low U and Th abundance in this sample. A single aliquot of Imperial Topaz Mine topaz ($Al_2SiO_4F_2$) yielded a small excess of ^{21}Ne (0.038 ± 0.001 fmol/g) and a larger excess of ^{22}Ne (1.86 ± 0.04 pmol/g). There are no known published measurements with which to compare these results.

8. Discussion and Conclusions

Accurate isotopic analysis of neon in minerals has historically been hindered by multiple isobars, in particular $^{40}Ar^{+2}$ affecting ^{20}Ne, ^{20}NeH affecting ^{21}Ne, and CO_2^{+2} affecting ^{22}Ne. The Helix-MC-*Plus*^{10K} mass spectrometer has sufficient mass resolution to fully resolve the isobars affecting the two lighter Ne isotopes. However, it does not have adequate mass resolution (>6000) to yield isobar free ^{22}Ne measurements. As shown here, by measuring ^{22}Ne on the low mass side of the CO_2^{+2}-^{22}Ne doublet in HR mode and by using the abundance of $^{45}CO_2^{+2}$ simultaneously measured on H2, it is possible to eliminate more than 99% of the isobar. This comes with two important trade-offs. First, sensitivity for all isotopes is reduced by slightly more than 50% relative to LR mode. In applications that are atom-limited for ^{21}Ne, which is typically by far the least abundant isotope in a neon analysis, there would be some degradation of precision as the number of ions counted is reduced. However, for many applications in cosmogenic and nucleogenic dating, the major limitation is analytical blank and/or the presence of atmospheric contamination in the sample. For such samples the reduction in total ions counted is likely irrelevant to overall precision. The second trade-off is the need to frequently relocate the required measurement point in the face of magnetic field or accelerating voltage drift. This can be accomplished with little time penalty by regularly scanning the dynamic CO_2^{+2} peak while pumping the mass spectrometer between analyses.

Flux-assisted fusion in Li borate at ~1100^{o}C quantitatively liberated neon from all minerals we have so far investigated, including silicates (quartz, pyroxene, zircon, topaz), phosphates (apatite), oxides (hematite), and fluorides (fluorite). This temperature is substantially lower than is required to extract neon without flux, with associated benefit in analytical blank and reduction in high temperature degradation of furnace elements. Although not attempted here, step-heating could be undertaken to improve neon component resolution (e.g., removal of atmosphere) at temperatures below the melting point of the flux (~900^{o}C), followed by flux fusion at 1100^{o}C. We have successfully applied the borate fusion technique for both He and Ne measurements (Farley and McKeon, 2015) and it is likely applicable for heavier noble gas extractions as well.

In the development of new extraction and purification techniques, and in comparing analytical results among laboratories, it is useful to have reference minerals. The ideal candidates would have high excess neon concentrations with high excess neon fractions, and would be homogenous at reasonable aliquot size. Both Cronus-A quartz and Cronus-P pyroxene are excellent candidates in this regard, as already noted for Cronus-A by Vermeesch et al. (2015). Both materials have easily measured concentrations of both ^{21}Ne and ^{22}Ne on samples of ~20-100 mg mass, and with large excesses relative to atmosphere (>80%, except just 18% for ^{22}Ne in Cronus-A).

Because nucleogenic neon is typically associated with very high concentrations of ^{4}He, a reference material for nucleogenic neon measurements should have ^{21}Ne/^{4}He~5x10^{-8} to establish that ^{4}He is not impacting the neon measurement. For that reason we analyzed

apatite, zircon, hematite, fluorite, and topaz samples. The apatite, zircon, and hematite samples all yielded readily measurable ^{21}Ne excesses with excess fractions of 0.85-0.999. In the case of Durango, a large excess of ^{22}Ne (from α capture by ^{19}F) was also measured. Although already widely used as a reference material for He dating applications, we found noticeable variability (±4% 1σ) in the excess neon concentrations in Durango apatite, possibly arising from the heterogeneity of U and Th in this material (Boyce and Hodges, 2005). A similar degree of heterogeneity was observed in the ^{21}Ne excesses of the CIT hematite standard. Further work is required to establish whether the variability in these specimens is inherent to the samples or arises from currently unknown analytical issues. The two analyses of SL1 zircon are highly reproducible and have extremely large excess ^{21}Ne concentration, thus making it a promising candidate for a reference material. In contrast, the topaz and fluorite we analyzed both had disappointingly low excess neon concentrations, suggesting they may not be useful as reference materials.

Despite elimination of the ^{22}Ne isobar in the Helix-MC-*Plus*^{10k}, it is notable that the ^{22}Ne excesses in the reference materials are more poorly reproduced than the ^{21}Ne excesses of similar size. For example, in the Cronus-A quartz, the standard deviation of the excess ^{22}Ne is ten times larger than that of the excess ^{21}Ne despite the excess ^{22}Ne/^{21}Ne ratio of 1.22. This almost certainly arises from the fact that atmosphere has almost 35 times more ^{22}Ne than ^{21}Ne, such that the correction of the measured Ne to obtain the excess is much larger for ^{22}Ne than ^{21}Ne. This observation underscores the need to further develop creative ways to reduce the atmospheric contamination of samples for neon analysis (e.g., Peron et al. (2019)), especially for improved ^{22}Ne quantification.

Acknowledgements

The authors thank Dan Barfod and two anonymous reviewers for helpful comments on this manuscript.

References

Avice, G., Belousov, A., Farley, K.A., Madzunkov, S.M., Simcic, J., Nikolic, D., Darrach, M.R., Sotin, C., 2019. High-precision measurements of krypton and xenon isotopes with a new static-mode quadrupole ion trap mass spectrometer. J. Anal. At. Spectrom. 34, 104–117. https://doi.org/10.1039/c8ja00218e

Blard, P.-H., Balco, G., Burnard, P.G., Farley, K.A., Fenton, C.R., Friedrich, R., Jull, A.J.T., Niedermann, S., Pik, R., Schaefer, J.M., Scott, E.M., Shuster, D.L., Stuart, F.M., Stute, M., Tibari, B., Winckler, G., Zimmermann, L., 2015. An inter-laboratory comparison of cosmogenic He-3 and radiogenic He-4 in the CRONUS-P pyroxene standard. Quat. Geochronol. 26, 11–19. https://doi.org/10.1016/j.quageo.2014.08.004

Boyce, J.W., Hodges, K.V., 2005. U and Th zoning in Cerro de Mercado (Durango, Mexico) fluorapatite: Insights regarding the impact of recoil redistribution of radiogenic He-4 on (U-Th)/He thermochronology. Chem. Geol. 219, 261–274.

Cox, S.E., Farley, K.A., Cherniak, D.J., 2015. Direct measurement of neon production rates by (alpha,n) reactions in minerals. Geochim. Cosmochim. Acta 148, 130–144. https://doi.org/10.1016/j.gca.2014.08.036

Eberhardt, P., Eugster, H.P., Marti, K., 1965. A redetermination of isotopic composition of atmospheric neon. Z. NATURFORSCHUNG PART -Astrophys. Phys. Phys. Chem. A 20, 623+.

Farley, K.A., Flowers, R.M., 2012. (U-Th)/Ne and multidomain (U-Th)/He systematics of a hydrothermal hematite from eastern Grand Canyon. Earth Planet. Sci. Lett. 359, 131–140. https://doi.org/10.1016/j.epsl.2012.10.010

Farley, K.A., McKeon, R., 2015. Radiometric dating and temperature history of banded iron formation–associated hematite, Gogebic iron range, Michigan, USA. Geology 43, 1083–1086. https://doi.org/10.1130/G37190.1

Fenton, C., Niedermann, S., M. Goethals, M., Schneider, B., Wijbrans, J.R., 2009. Evaluation of cosmogenic 3He and 21Ne production rates in olivine and pyroxene from two Pleistocene basalt flows, western Grand Canyon, AZ, USA. Quatemary Geochronol. 4, 475–492. https://doi.org/10.1016/j.quageo.2009.08.002

Gautheron, C.E., Tassan-Got, L., Farley, K.A., 2006. (U-Th)/Ne chronometry. Earth Planet. Sci. Lett. 243, 520–535. https://doi.org/10.1016/j.epsl.2006.01.025

Hiyagon, H., 1989. Neon isotope measurement in the presence of helium. Mass Spectrosc. 37, 325–330.

Honda, M., McDougall, I., Patterson, D., Doulgeris, A., Clague, D., 1991. Possible solar noble-gas component in Hawaiian basalts. Nature 349, 149–151.

Honda, M., Zhang, X., Phillips, D., Hamilton, D., Deerberg, M., Schwieters, J.B., 2015. Redetermination of the 21Ne relative abundance of the atmosphere, using a high resolution, multi-collector noble gas mass spectrometer (HELIX-MC Plus). Int. J. Mass Spectrom. 387, 1–7. https://doi.org/10.1016/j.ijms.2015.05.012

House, M.A., Farley, K.A., Stockli, D.F., 2000. Helium chronometry of apatite and titanite using Nd-YAG laser heating. Earth Planet. Scince Lett. 183, 365–368.

McDowell, F.W., McIntosh, W.C., Farley, K.A., 2005. A precise Ar-40-Ar-39 reference age for the Durango apatite (U-Th)/He and fission-track dating standard. Chem. Geol. 214, 249–263. https://doi.org/DOI 10.1016/j.chemgeo.2004.10.002

Nasdala, L., Corfu, F., Schoene, B., Tapster, S.R., Wall, C.J., Schmitz, M.D., Ovtcharova, M., Schaltegger, U., Kennedy, A.K., Kronz, A., Reiners, P.W., Yang, Y.-H., Wu, F.-Y., Gain, S.E.M., Griffin, W.L., Szymanowski, D., Chanmuang N., C., Ende, M., Valley, J.W., Spicuzza, M.J., Wanthanachaisaeng, B., Giester, G., 2018. GZ7 and GZ8 – Two Zircon Reference Materials for SIMS U-Pb Geochronology. Geostand. Geoanalytical Res. 42, 431–457. https://doi.org/10.1111/ggr.12239

Nelder, J., Mead, R., 1965. A Simplex-method for function minimization. Comput. J. 7, 308–313. https://doi.org/10.1093/comjnl/7.4.308

Niedermann, S., 2002. Cosmic-ray-produced noble gases in terrestrial rocks: Dating tools for surface processes, in: Porcelli, D., Ballentine, C.J., Wieler, R. (Eds.), Noble Gases in Geochemistry and Cosmochemistry. Mineralogical Society of America, Washington D.C., p. 844.

Niedermann, S., Graf, T., Marti, K., 1993. Mass spectrometric identification of cosmic-ray produced neon in terrestrial rocks with multiple meom components. Earth Planet. Sci. Lett. 118, 65–73.

Olsen, D., 1971. Origin of topaz deposits near Ouro-Prieto, Minas Gerais, Brazil. Econ. Geol. 66, 627-. https://doi.org/10.2113/gsecongeo.66.4.627

Peron, S., Moreira, M.A., Kurz, M.D., Curtice, J., Blusztajn, J.S., Putlitz, B., Wanless, V.D., Jones, M.R., Soule, S.A., Mittelstaedt, E., 2019. Noble gas systematics in new popping rocks from the Mid-Atlantic Ridge (14 degrees N): Evidence for small-scale upper mantle heterogeneities. EARTH Planet. Sci. Lett. 519, 70–82. https://doi.org/10.1016/j.epsl.2019.04.037

Sarda, P., Staudacher, T., Allegre, C.J., 1988. Neon isotopes in submarine basalts. Earth Planet. Sci. Lett. 91, 73–88.

Schafer, J., Ivy-Ochs, S., Wieler, R., Leya, I., Baur, H., Denton, G., Schluchter, C., 1999. Cosmogenic noble gas studies in the oldest landscape on earth: surface exposure ages of the Dry Valleys, Antarctica. Earth Planet. Sci. Lett. 167, 215–226.

Sole, J., Pi, T., 2006. Determination of the Ne-22(nucl)/He-4(rad) ratio in natural uranium-rich fluorite by mass spectrometry. Phys. Rev. C 74. https://doi.org/047601 10.1103/PhysRevC.74.047601

Vermeesch, P., Balco, G., Blard, P.-H., Dunai, T.J., Kober, F., Niedermann, S., Shuster, D.L., Strasky, S., Stuart, F.M., Wieler, R., Zimmermann, L., 2015. Interlaboratory comparison of cosmogenic Ne-21 in quartz. Quat. Geochronol. 26, 20–28. https://doi.org/10.1016/j.quageo.2012.11.009

Wielandt, D., Storey, M., 2019. A new high precision determination of the atmospheric 21Ne abundance. J Anal Spectrom 34, 535–549. https://doi.org/10.1039/C8JA00336J

Yatsevich, I., Honda, M., 1997. Production of nucleogenic neon in the Earth from natural radioactive decay. J. Geophys. Res. 102, 10,291-10,298.

Young, J., 1990. Fluorite Deposits of Westmoreland, New Hampshire. Rocks Miner. 65, 328–335. https://doi.org/10.1080/00357529.1990.11761691

Zhang, X., Honda, M., Hamilton, D., 2016. Performance of the High Resolution, Multi-collector Helix MC Plus Noble Gas Mass Spectrometer at the Australian National University. J. Am. Soc. Mass Spectrom. 27, 1937–1943. https://doi.org/10.1007/s13361-016-1480-3

Figure Captions

Figure 1. Flow chart for set-up and operation of the Helix-MC-*Plus*^{10k} in HR mode.

Figure 2. Mass spectrum of a triple shot of the air standard on the Helix-MC-*Plus*^{10k} using the smallest defining slit (HR mode). Legend indicates which CDD detector was being used to measure the species labelled on each trace. The vertical hatching indicates the target region for simultaneous neon measurement, with ^{22}Ne being measured on the low-mass-side pure ^{22}Ne bench of the ^{22}Ne-CO_2^{+2} doublet. Note the clear separation of ^{20}Ne from $^{40}Ar^{+2}$ on the low mass side and ^{20}HF-$^{20}H_2O$ on the high mass side using the high mass resolution L1 detector.

Figure 3. Low mass side of the ^{22}Ne-CO_2^{+2} doublet measured on the H1 detector in HR mode plotted at two different scales. Black spectrum was measured on a triple shot of the ^{22}Ne spike, while the blue curve was measured on an evacuated mass spectrometer, i.e., in dynamic mode. Spectra are normalized to the highest measured value to allow plotting on the same scale. Panel A) indicates the 50% point of the dynamic CO_2 peak (M_C), the desired measure point (M_R) and the offset between them (ΔM). Panel B) defines the target zone for ^{22}Ne measurement: it must lie to the high mass side of the 99% point of the ^{22}Ne beam, and to the low mass side of 10% point on the normalized dynamic CO_2 peak.

Figure 4. Pressure linearity of the neon peak height response of the Helix-MC-*Plus*^{10k} mass spectrometer. Across the total range in ^{20}Ne in the mass spectrometer from $7x10^{-12}$ to $3x10^{-10}$ cc STP there is no detectable change in sensitivity (i.e., no peak-height nonlinearity).

Figure 5. Results of 35 furnace hot blank measurements made in HR mode. The x-axis indicates the measured amount of ^{20}Ne in each blank. The Y-axis indicates the residual mass 22 remaining after subtraction of the amount of ^{22}Ne expected from the measured ^{20}Ne assuming atmospheric isotopic composition for the blank. This residual is a measure of how much CO_2^{+2} is inadvertently still being detected using the scheme described in Figure 1. Measurements indicate that >99.5% of the CO_2^{+2} present in the doublet is rejected.

Table 1 Tuning Conditions and Characteristics

Parameter	LR Mode (large defining slit)	HR Mode (small defining slit)
Trap Current	*400*	*400*
AV	*9900*	*9900*
Extraction Symmetry	2.47	29.25
Extraction Focus	33.08	27.94
Trap voltage	85.88	80.53
Electron Energy	134.24	139.52
Ion Repeller	-2.59	-5.42
Horizontal Symmetry	-5.18	26.34
Extraction Lens	36.2	60.75
Flatapole	*2*	0.827
Rotation Quad	*6.73*	2.4531
Vertical Deflection N	*55*	45.025
Vertical Deflection S	*87*	72.792
Items in Italics - not optimized		
^{20}Ne Sensitivity		
cps/pcc	578	270
cps/fmol	12950	6048
amps/torr @ 3.75 liters	4.56E-04	2.13E-04
Mass Resolving Power		
95%-5% definition		10300

Table 2

Sample	Mass (g)	^{20}Ne fmol/g	±	^{21}Ne/^{20}Ne	±	^{22}Ne/^{20}Ne	±	F^{21}Ne$_{xs}$	^{21}Ne$_{xs}$ fmol/g	±	F^{22}Ne$_{xs}$	^{22}Ne$_{xs}$ fmol/g	±
Cosmogenic Neon													
Quartz	0.12685	30.85	0.69	0.0208	0.0008	0.1222	0.0043	0.860	0.5522	0.0205	0.165	0.6235	0.1527
Cronus-A	0.12013	28.03	0.63	0.0227	0.0009	0.1267	0.0045	0.872	0.5542	0.0202	0.195	0.6911	0.1410
(125-250 um)	0.24622	32.69	0.34	0.0198	0.0003	0.1228	0.0026	0.853	0.5509	0.0073	0.169	0.6801	0.1000
						weighted average and SEM			***0.5510***	***0.0065***		***0.67***	***0.07***
								Mat/g	***331.7***	***3.9***		***403.3***	***42.1***
Pyroxene	0.04960	5.097	0.076	0.4752	0.0095	0.6324	0.0176	0.994	2.406	0.032	0.839	2.703	0.077
Cronus-P	0.02642	7.929	0.122	0.3064	0.0062	0.4428	0.0171	0.990	2.406	0.032	0.770	2.702	0.128
(125-250 um)						***weighted average and SEM***			***2.406***	***0.023***		***2.700***	***0.065***
								Mat/g	***1448***	***14***		***1625***	***39***
Nucleogenic Neon													
Hematite	0.02062	7.116	0.076	0.1221	0.0019	0.1161	0.0018	0.976	0.8478	0.0097	0.121	0.1002	0.0117
CIT-10443	0.02088	10.83	0.11	0.0832	0.0013	0.1046	0.0016	0.965	0.8689	0.0100	0.025	0.0281	0.0166
(90-500 um)	0.02012	158.5	1.7	0.0089	0.0001	0.1014	0.0016	0.673	0.9464	0.0158	-0.006	-0.0949	0.2603
	0.02062	26.07	0.27	0.0374	0.0006	0.1097	0.0023	0.922	0.9003	0.0107	0.071	0.2019	0.0666
	0.02022	12.92	0.17	0.0733	0.0013	0.1064	0.0035	0.960	0.9100	0.0117	0.041	0.0565	0.0562
	0.02010	6.983	0.101	0.1342	0.0025			0.978	0.9172	0.0114	ND	ND	ND
	0.02012	142.2	1.6	0.0095	0.0001	0.1035	0.0017	0.694	0.9377	0.0154	0.014	0.2076	0.2493
	0.02018	74.19	0.88	0.0153	0.0002	0.1044	0.0018	0.810	0.9213	0.0131	0.023	0.1744	0.1410
	average					***weighted average and SEM***			***0.9050***	***0.0120***		***0.0810***	***0.026***
Apatite	0.09981	6.525	0.069	0.0596	0.0009	1.456	0.022	0.951	0.3701	0.0043	0.930	8.837	0.101

Durango-C	0.10100	4.703	0.182	0.0805	0.0045	1.979	0.108	0.964	0.3649	0.0154	0.948	8.825	0.358
(104-212 um)	0.03026	8.780	0.131	0.0479	0.0010	1.165	0.026	0.939	0.3946	0.0057	0.912	9.329	0.171
	0.01461	12.03	0.19	0.0361	0.0008	0.8999	0.0256	0.919	0.3994	0.0061	0.887	9.601	0.258
	average					***weighted average and SEM***			***0.3840***	***0.0090***		***9.130***	***0.200***
Zircon	0.00547	47.37	0.71	1.477	0.029	0.1150	0.0111	0.998	69.83	0.92	0.113	0.6151	0.6786
SL1	0.01064	19.66	0.30	3.570	0.072	0.1565	0.0140	0.999	70.12	0.92	0.348	1.071	0.318
<190 um	**average**					***weighted average and SEM***			***70.00***	***0.65***		***0.99***	***0.29***
Fluorite	0.10206	2.258	0.075	0.0029	0.0002	0.2637	0.0130	0.008	0.0001	0.0006	0.613	0.3653	0.0248
W-90	0.09709	1.797	0.019	0.0030	0.0001	0.2910	0.0044	0.035	0.0002	0.0001	0.649	0.3395	0.0059
(104-212 um)	**average**					***weighted average and SEM***			***0.0002***	***0.0001***		***0.3410***	***0.0050***
Topaz - *ITP-A*	0.04997	14.32	0.15	0.0055	0.0001	0.2322	0.0035	0.474	0.0375	0.0011	0.561	1.865	0.038
(104-212 um)													

$F^{21}Ne_{xs}$ - fraction of neon isotope that is non-atmospheric

Mat/g - millions of atoms per gram

ND - not determined, measurement lost

SEM - weighted standard error of the mean

Declaration of competing interests

☐ The authors declare that they have no known competing financial interests or personal relationships that could have appeared to influence the work reported in this paper.

☒The authors declare the following financial interests/personal relationships which may be considered as potential competing interests:
Author Doug Hamilton is employed by ThermoFisher the manufacturer of the mass spectrometer described in this manuscript.

Neon Analysis Flow Chart

Initial setup

1. Set approximate detector positions for neon and CO_2^{+2} measurement on L1, AX, H1, H2.

2. Tune for maximum sensitivity on ^{20}Ne in L1.

3. Tune for maximum mass resolving power on ^{22}Ne in H1. MRP should exceed 10,000.

4. Scan the dynamic CO_2^{+2} peak at ~ 1 mAMU resolution and determine the peak height.

5. From the scan in step 4, determine the magnetic mass associated with the 50% point on the low mass side (M_C) of the dynamic CO_2^{+2} peak.

6. From the scan in step 4, determine the magnetic mass where the desired degree of rejection of CO_2^{+2} occurs on the low mass side (M_R). These two steps define the magnetic offset from the 50% point to the measure point ($\Delta M=M_C-M_R$).

7. Position the L1, AX, and H2 ($^{45}CO_2^{+2}$) detectors so that the neon isotopes are aligned at M_R. Of course H1 will be set on the very low mass side of the ^{22}Ne peak (Figure 1). Note that since the AX detector cannot be moved it may be necessary to adjust the position of H1 and relocate M_R so as to get proper alignment of ^{21}Ne on AX.

Operation

8. Perform dynamic CO_2^{+2} scan to relocate the position of the 50% point (M_c). Set the magnetic field to $M_c-\Delta M$. This is the current position of the measure point M_R; this step is done to accommodate magnetic field drift.

9. Close the mass spectrometer pump-out valve, measure the ratio of $CO_2^{+2}/^{45}CO_2^{+2}$ (R_c = H1/H2). This should be done fairly quickly, so as to minimize ingrowth of ^{22}Ne from instrument memory.

10. Pump mass spectrometer for at least a few minutes, and then admit unknown or standard for analysis.

11. Without adjusting magnetic field, measure H2, H1, AX, and L1 for desired period (typically ~30 minutes) in 30 second integrations. In addition to the usual time and peak height data written to the data file for this run, also include the most recent value of R_c.

12. Before performing time zero regressions (or ratio regressions), correct the ^{22}Ne in each integration for the remaining isobaric CO_2^{+2} at the measure point: $^{22}Ne=H1-RC*H2$

13. Pump mass spectrometer for at least several minutes, go to step 8.

Figure 1

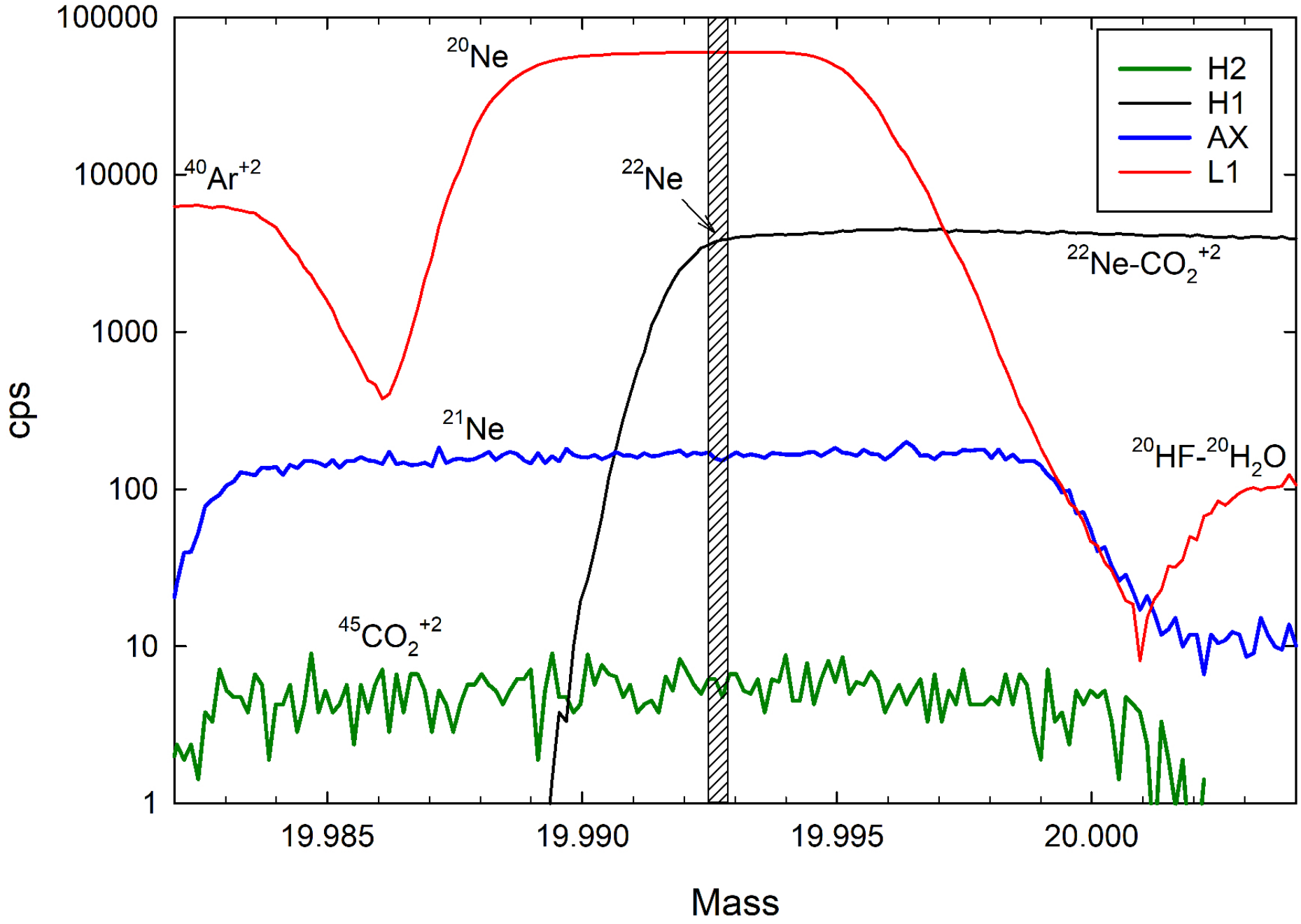
100000
10000
1000
100
10
1
cps
19.985
19.990
19.995
20.000
Mass
H2
H1
AX
L1
^{20}Ne
^{40}Ar^{+2}
^{22}Ne
^{22}Ne-CO$_2$$^{+2}$
^{21}Ne
^{20}HF-^{20}H$_2$O
^{45}CO$_2$$^{+2}$

Figure 2

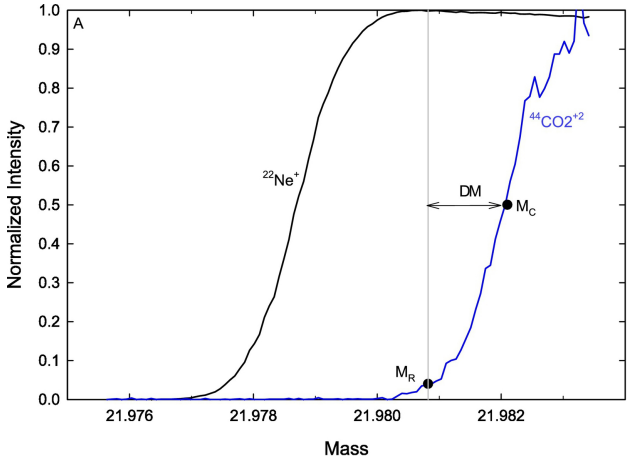
A
Normalized Intensity
Mass
$^{22}Ne^{+}$
$^{44}CO2^{+2}$
DM
M_C
M_R
1.0
0.9
0.8
0.7
0.6
0.5
0.4
0.3
0.2
0.1
0.0
21.976
21.978
21.980
21.982

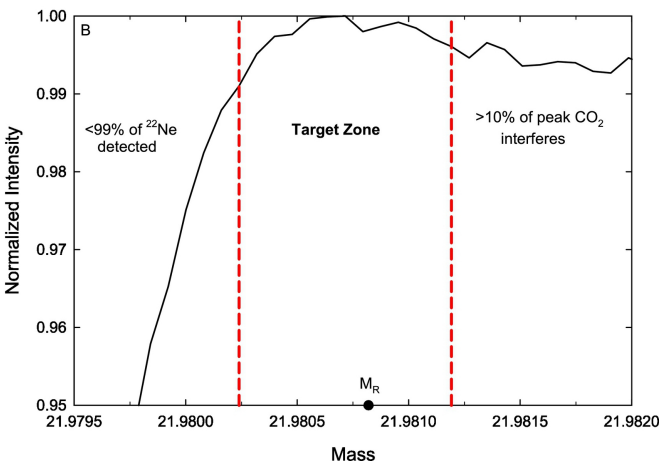
B
Normalized Intensity
Mass
<99% of ^{22}Ne detected
Target Zone
>10% of peak CO_2 interferes
M_R
1.00
0.99
0.98
0.97
0.96
0.95
21.9795
21.9800
21.9805
21.9810
21.9815
21.9820

Figure 3

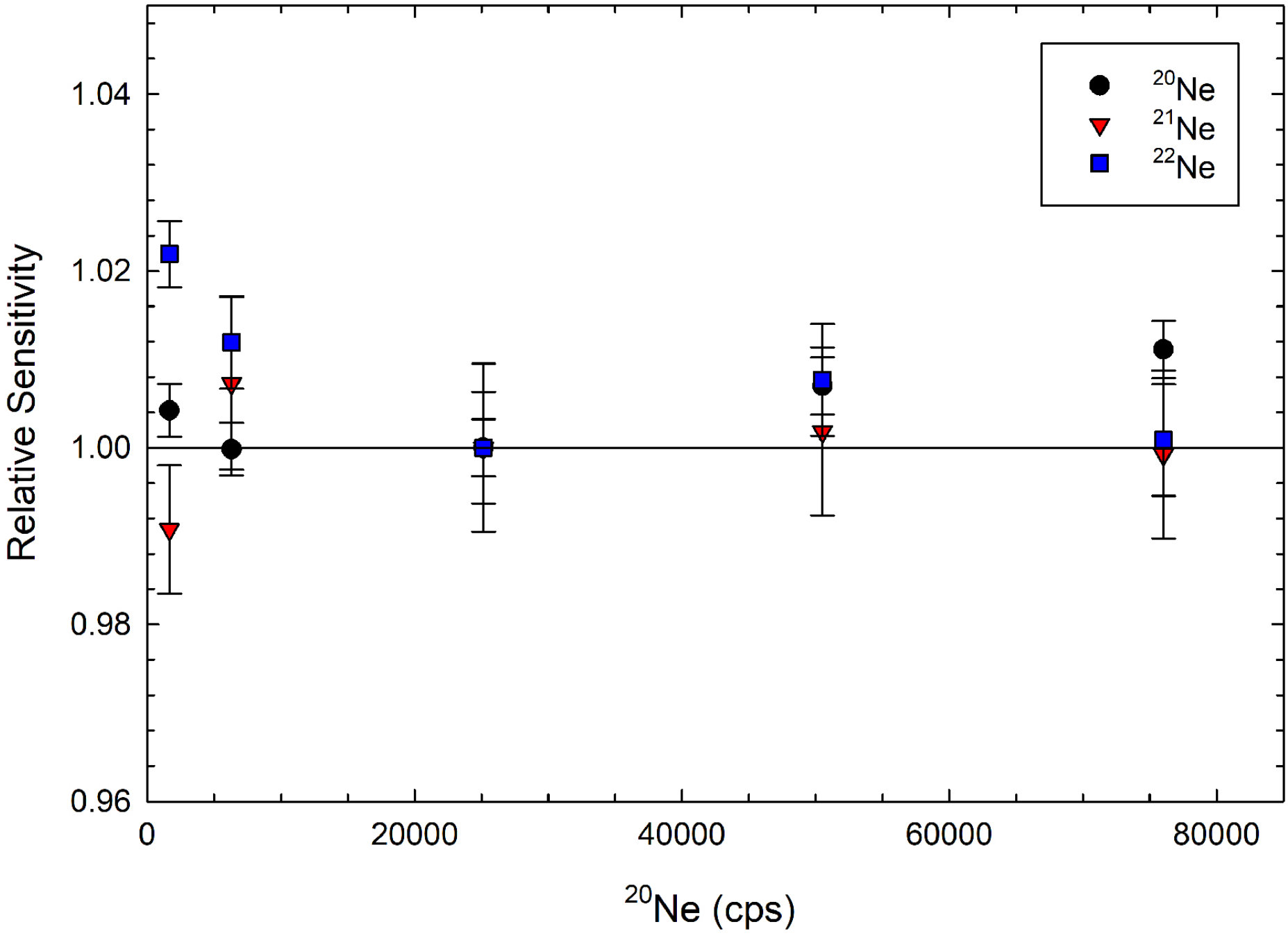
Relative Sensitivity
1.04
1.02
1.00
0.98
0.96
0
20000
40000
60000
80000
^{20}Ne (cps)
^{20}Ne
^{21}Ne
^{22}Ne

Figure 4

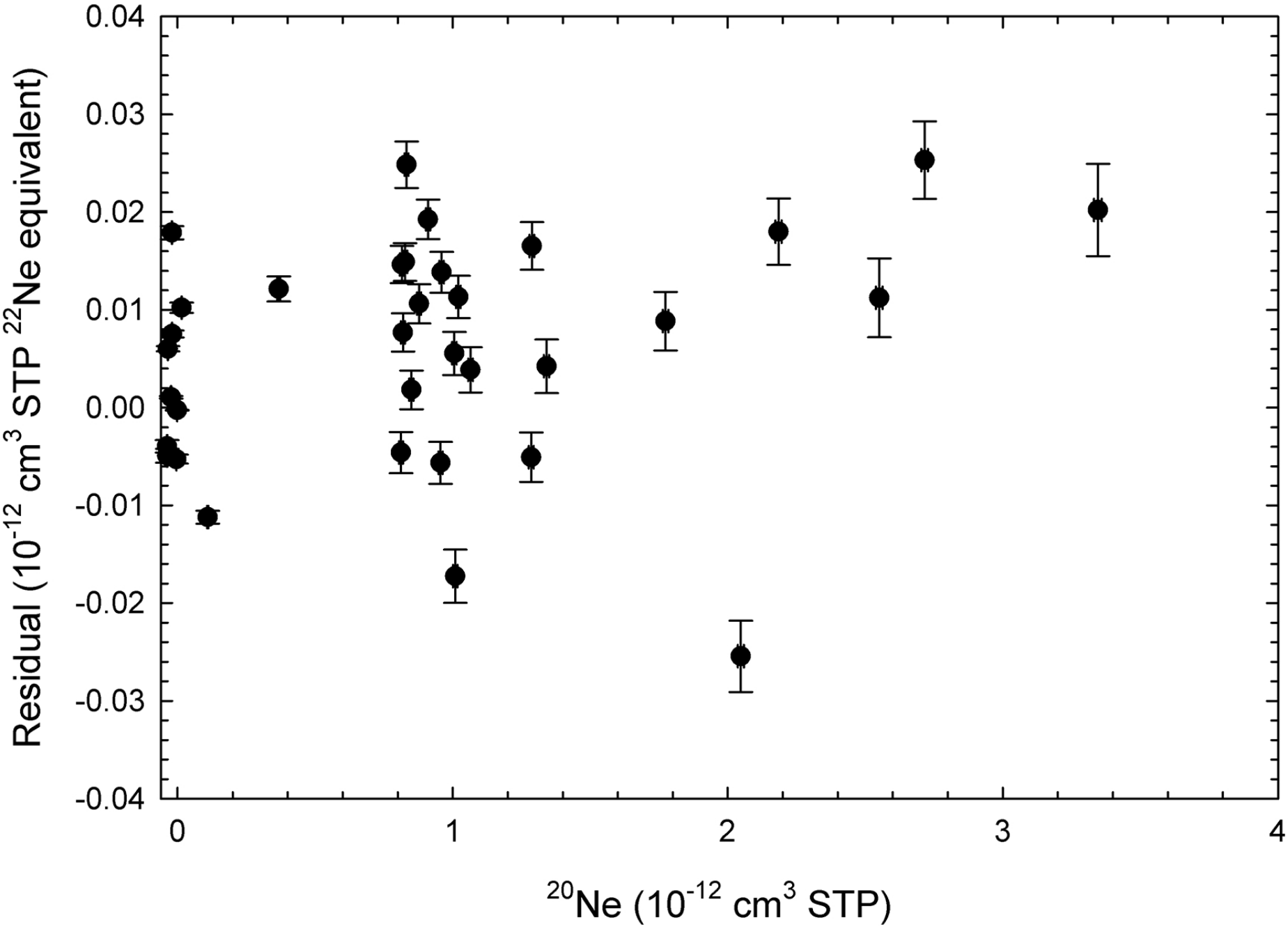
0.04
0.03
0.02
0.01
0.00
-0.01
-0.02
-0.03
-0.04
Residual (10^{-12} cm^3 STP ^{22}Ne equivalent)
0
1
2
3
4
^{20}Ne (10^{-12} cm^3 STP)

Figure 5